

# Liquid interfaces in viscous straining flows: Numerical studies of the selective withdrawal transition

By MARKO KLEINE BERKENBUSCH<sup>1†</sup>, ITAI COHEN<sup>2‡</sup>  
AND WENDY W. ZHANG<sup>1¶</sup>

<sup>1</sup>Department of Physics & James Franck Institute, The University of Chicago, 5640 S. Ellis Avenue, Chicago IL 60637, USA

<sup>2</sup>Current Address: Physics Department, Cornell University, Ithaca, NY 14853, USA

(Received 26 February 2019)

In selective withdrawal, the interface between two liquid layers is deformed by an imposed withdrawal flow. A shape transition occurs at a threshold flow rate that changes the topology of the interface from a steady-state hump to an entrained spout. Near the transition a very sharp hump tip occurs, with the minimum tip radius far smaller than the characteristic lateral length-scale. Previous measurements (Cohen & Nagel (2002)) suggest the sharp hump is created via an approach towards a singular steady-state shape which is cut off at a small lengthscale. To help unfold the mechanism underlying the shape transition and to determine the origin of the cutoff lengthscale, we construct a numerical model of selective withdrawal. Its results are consistent with experimental measurements, but it has a larger dynamic range near the transition. The increased range enables us to identify the shape transition as a saddle-node bifurcation. The transition does not involve an approach towards a singular shape. At threshold, the hump radius is comparable to the hump height. We also analyze selective withdrawal under a variety of withdrawal conditions and find that the different results collapse when the lengthscales are appropriately rescaled.

---

## 1. Introduction

Recently, there has been an explosion of effort in creating microfluidic devices that use the generation, transport and coalescence of liquid drops to mix, assay and conduct controlled reactions with dilute amounts of reactants (Song *et al.* (2003); Tice *et al.* (2004); Joanicot & Ajdari (2005); Chen *et al.* (2005); Lucchetta *et al.* (2005); Cristini & Tan (2004); Hansen *et al.* (2002)). These devices can also be used to manufacture novel materials such as monodisperse emulsions (Takeuchi *et al.* (2005); Ganan-Calvo & Gordillo (2001); Utada *et al.* (2005); Umbanhowar *et al.* (2000)), foams (Lorenceanu *et al.* (2005); Garstecki *et al.* (2005*b,a*)) and photonic band gap crystals (Wolfe *et al.* (2004); Domachuk *et al.* (2004)). A crucial step in all these emerging applications is the generation of a liquid drop from an interface that spans across the microfluidic channel. In devices that use “flow-focusing”, the interface is distorted by an external flow, eventually breaking up into droplets (Shelley *et al.* (2003)). Usually there is no clear understanding of how different

† mkb@uchicago.edu

‡ ic64@cornell.edu

¶ wzhang@uchicago.edu

factors such as the geometry of the channel, the flow speed and the reservoir pressure interact with the flow dynamics, as characterized by the viscosity of the drop and the surrounding liquid and surface tension, to determine the drop size. Here we consider how the characteristic lengthscale of interface deformation depends on boundary conditions by examining selective withdrawal, a large-scale experiment which reproduces the important physical processes in flow-focusing microfluidic devices.

In the selective withdrawal experiment (Cohen (2004); Cohen & Nagel (2002)), two viscous, immiscible fluids are layered vertically in a large container. When the upper fluid is withdrawn through a tube, the horizontal liquid-liquid interface is deformed into a steady-state hump. When the flow rate is increased above a certain threshold, the interface undergoes a transition from a hump to an entrained spout. Both liquids are viscous so that the hump shape is determined by viscous stresses in the two liquids and surface tension, just as occurs in a microfluidic channel. Gravity is significant on larger length-scales and serves primarily to keep the interface flat away from the hump. Measurements of the hump height and curvature suggest that the sharp hump is created via an approach towards a steady-state singular shape. This behavior is qualitatively very different from what is known about drop breakup in viscous straining flows in emulsification studies (Taylor (1934); Grace (1982); Rallison & Acrivos (1978); Stone (1994)). Even though the stress balancing mechanisms are closely related, drops in extensional flows are found to be able to sustain only slight deformations with rounded ends when the viscosities of inner and outer fluid are roughly matched.

This apparent disparity in the interface deformation dynamics in two systems subjected to the same physical processes but different boundary conditions motivates our analysis. In the present work, we investigate the properties of the selective withdrawal system in the vicinity of the steady-state hump to entrained spout transition. Using a boundary integral simulation of viscous flows, we set up a simplified numerical model of the hump state and use this to study the system below and close to the entrainment threshold. By simulating the dynamics in the model system, we are able to obtain steady-state shapes at flow rates much closer to the threshold flow rate than the experiment. We find that the hump state vanishes in a saddle-node bifurcation at the threshold flow rate. This transition does not involve an approach towards a singular shape. The radius of the hump tip remains comparable with the hump height. A comparison of the numerical results with experimental measurements shows that the measurements are also consistent with our interpretation of the transition as a saddle-node bifurcation. Finally, we analyze hump-to-spout transition dynamics with different boundary conditions and different kinds of withdrawal flows. While changing the boundary conditions led to significant changes in the interface shape at the transition, the tip radius of curvature remained comparable to the hump height for all the cases examined.

These results are relevant not only in applications involving microfluidic channels. There are ongoing efforts to use the thin, steady-state spout formed by the imposed withdrawal to coat particles (Cohen *et al.* (2001)) and biological cells (Wyman *et al.* (2004)), and to form thin glass fibers (Ganan-Calvo *et al.* (2004); Fitt *et al.* (2001)).

Mathematically, the possibility that a hump of arbitrarily large curvature at its tip can be formed at a finite flow rate corresponds to the formation of a steady-state singularity across a topological transition in viscous two-phase flow. The possible formation of singularities is a general question that arises in many different contexts, from theories for the formation of stars (Chandrasekar (1967)) to nuclear fission (Bohr (1939)). In two-phase flow, there have been many recent studies of the formation of finite-time singularities, which, for example, occur in surface-tension driven breakup of a liquid drop (cf. Eggers (1997); Cohen *et al.* (1999); Zhang & Lister (1999); Sierou & Lister

(2003); Leppinen & Lister (2003); Chen & Steen (1997); Doshi *et al.* (2003)). In comparison, the possibility that the combined effect of surface tension and an external flow can create steady-state singularities at a finite threshold flow rate has received less attention (Joseph *et al.* (1991); Jeong & Moffatt (1992)).

More generally, topological transitions in the steady-state interface analogous to the hump-spout transition observed in selective withdrawal arise in many different contexts, for example the deposition of trailing droplets by a drop sliding down an incline (Limat & Stone (2004)) or the formation of humps and jets on an interface under laser illumination (Casner & Delville (2001)). Two particularly striking examples are topological transitions driven by surfactant effects (De Bruijn (1993); Eggleton *et al.* (2001); Fernandez & Homsy (2003, 2004); Krechetnikov & Homsy (2004)), or by electric fields, for example Taylor cone formation (Taylor (1964*b*); Li *et al.* (1994); Zubarev (2002); Reznik *et al.* (2004)). This visual similarity raises the possibility that the dynamics associated with topological transitions in these disparate problems may share certain fundamental similarities, and therefore can be classified into a small number of distinct classes. The close examination of the selective withdrawal experiment presented here constitutes our first step towards answering this question.

The rest of the paper is organized as follows: we describe both the selective withdrawal experimental results and emulsification study results in more detail in section 2. In section 3 we present a simplified model for the selective withdrawal experiment. Section 4 discusses how the simplified model is implemented and solved via a boundary integral simulation. Section 5 focuses on the behavior of the steady-state interface near the entrainment threshold. Numerical results showing the existence of a saddle-node bifurcation in the interface solution at threshold are presented and compared against experimental measurements. In addition, we also describe a simple physical mechanism that accounts for the existence of the saddle-node bifurcation. In section 6, we analyze how the steady-state interface changes as a function of the imposed flow rate. Finally, we discuss questions raised by results of our study and its relevance to other free-boundary problems in which a topological transition occurs in the steady-state interface (section 7) and reiterate our main findings in the conclusion (section 8).

## 2. Background

In the selective withdrawal experiment, a tube is inserted in the upper fluid with its tip suspended above the interface. When a flow is induced in the system by withdrawing the upper fluid through the tube, the interface is deformed upwards. At low flow rates  $Q$ , an axisymmetric steady-state hump with a stagnation point at the hump tip is formed. As the flow rate is increased, the tip rises higher above the neutral interface level and the curvature at the tip increases. When  $Q$  surpasses a certain threshold  $Q_c$ , the interface undergoes a transition in which the lower fluid becomes entrained in a thin axisymmetric spout along with the upper fluid. Once the spout has formed, an increase in  $Q$  causes the spout to thicken. Cohen and Nagel have analyzed the structure of these steady state tips near the entrainment threshold  $Q_c$ . They find that, almost independent of material parameters such as viscosity or density contrast, the surface shapes approach a highly curved, cusp-like configuration. Effects of Marangoni stresses due to varying surfactant concentrations have been studied and ruled out experimentally (Cohen (2001)). Measurements of the hump height and radius of curvature are consistent with an interpretation that, as the threshold is approached, the steady-state interface approaches a singular shape. Very close to the transition, the approach is cut off and no singular shape is observed in the experiment (Cohen & Nagel (2002); Cohen (2004)). In particular, Cohen

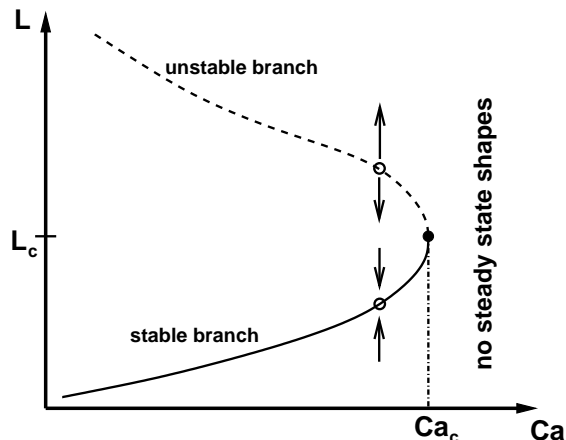


FIGURE 1. Bifurcation diagram for drop breakup in viscous straining flows

and Nagel report that, as the flow rate approaches the threshold value, the tip curvature appears to diverge with a powerlaw exponent of roughly  $-0.75$  while the hump height approaches its saturation value with a powerlaw exponent of  $0.64$ . The nontrivial scaling exponents suggest that the approach of the interface towards a singular shape can be described by a similarity solution of the second kind (Barenblatt (1996)). Such a solution retains a memory of boundary conditions at large lengthscales even as the characteristic lengthscale of the interface becomes very small.

A shape transition analogous to the selective withdrawal transition occurs when a liquid drop is emulsified into several drops by a straining flow. Taylor's 1934 pioneering study (Taylor (1934)) investigated how the threshold strain rate and threshold shape change as the viscosity contrast is varied.

When the viscosity of the drop,  $\mu_0$ , is equal to that of the ambient liquid,  $\mu$ , the threshold shape is a slightly deformed sphere. For  $\mu_0 \ll \mu$ , on the other hand, the threshold shape is a long slender drop with conical tips. Subsequent long-wavelength analyses and experiments show that in this limit the aspect ratio of the threshold shape scales as  $\sqrt{\lambda}$ , where  $\lambda$  is the viscosity ratio  $\mu_0/\mu$  (Taylor (1964a); Buckmaster (1973); Acrivos & Lo (1978)). In addition, the long-wavelength analyses show the bursting apart of the drop corresponds to a saddle-node bifurcation (Strogatz (1994)) in the steady-state shape. Below the threshold strain rate two steady-state drop shapes exist, one linearly stable and one linearly unstable. Above the threshold strain rate, no steady-state drop shape is possible. At the threshold strain rate, the unstable and stable shapes coincide and annihilate each other. This is illustrated in figure 1, which plots the length  $L$  of the steady-state drop as a function of the dimensionless strain rate  $Ca$ . The capillary number is defined as  $Ca = \mu E a / \gamma$ , where  $E$  is the dimensional imposed strain rate,  $a$  the radius of the undisturbed drop and  $\gamma$  surface tension. The most generic way for the two branches to merge smoothly at  $Ca_c$  is to form a horizontal parabola centered at  $(Ca_c, L_c)$ , where  $Ca_c$  is the dimensionless threshold strain rate and  $L_c$  is the threshold drop length. Consequently, the drop length of the stable shape near  $Ca_c$  scales like  $L_c - L_{\text{stable}} \propto \sqrt{Ca_c - Ca}$ .

While the long-wavelength analysis gives no information on how the tip curvature  $\kappa$  evolves as a function of  $Ca$ , both experiments and numerics show that it increases dramatically as  $Ca$  approaches  $Ca_c$  (Stone (1994); Hu *et al.* (2000)). For more moderate viscosity ratios  $\lambda \approx 1$  the tip curvature of the threshold drop shape  $\kappa_c$  remains on the

order of the drop size (Rallison & Acrivos (1978); Grace (1982); Rallison (1984)). More recently, a phenomenological model which describes the bursting of a viscous drop as a saddle-node bifurcation has been proposed (Navot (1999)) and shown to be consistent with numerical results (Blawdziewicz *et al.* (2002)).

In short, there appear to be two possible scenarios for how the steady-state hump transforms into a steady-state spout. The experimental measurements suggest an approach to a singular shape which is cut off very close to the transition, analogous to a weakly first-order phase transition. In contrast, theory, experiment and numerics on emulsification suggest a steady-state shape in a withdrawal flow should vanish via a saddle-node bifurcation, without approaching a singular shape. To resolve which of the two possible transition dynamics actually occurs in selective withdrawal, we construct a numerical model that reproduces key features of the experimental system but also enables us to approach much closer to the threshold flow rate.

### 3. Modeling selective withdrawal

Figure 2 shows a schematic of the selective withdrawal experiment: a cylindrical pipe is suspended over the horizontal interface between two fluids. The upper fluid is withdrawn through the pipe, creating a converging flow that deforms the free surface. A box is drawn around the region of significant interface deformation and the approximate shape of flow lines in the system is indicated.

The setup of the selective withdrawal experiment closely corresponds to a numerical study by Lister (Lister (1989)), which analyzed the onset of entrainment in two viscous layers with equal viscosities. In the numerical model, the withdrawal flow is driven by a point sink located in the upper layer. The interface is stabilized by both surface tension effects and gravity. Lister’s study focused on how the threshold flow rate depends on the material parameters and sink height, with particular emphasis on the role of surface tension. There was no analysis of the dynamics near the transition, nor how boundary conditions on the interface affects the dynamics.

Our numerical model is illustrated in figure 3. As in the Lister study, we mimic the withdrawal flow in the upper fluid by a point sink located at a distance  $S$  from the surface  $S_R$ . Unlike this previous study, we model the effect of a large reservoir below the interface by two conditions. First, we require that the fluid interface  $S_I$  between fluids 1 and 2 is pinned at  $S_R$  at a fixed radial distance  $a$ . Second, the pinning plane  $S_R$  is held at a constant pressure  $p_0$  such that fluid 1 is allowed to pass through  $S_R$  freely. We will show later that the second condition is not crucial.

An axisymmetric coordinate system as indicated in the figure is used throughout this study. In the low Reynolds-number limit fluid inertia becomes negligible and the flows in the system are governed by the Stokes equation for Newtonian incompressible fluids:

$$\nabla \cdot \sigma_i = -\nabla p_i + \mu_i \nabla^2 \mathbf{u}_i = \mathbf{0}, \quad \nabla \cdot \mathbf{u}_i = 0 \quad (3.1)$$

( $i=1,2$ ), where  $\mathbf{u}_i$  is the velocity field,  $p_i$  is the pressure,  $\mu_i$  is the viscosity and  $\sigma_i$  is the rate-of-strain field of the respective fluid.

Fluid 1 is bounded by its interface with fluid 2,  $S_I$ , and the constant pressure reservoir surface  $S_R$ . The boundary condition imposed on  $S_R$  is that of a constant normal stress jump of size  $p_0$ :

$$\mathbf{n} \cdot \sigma_1(\mathbf{x}) = p_0 \text{ for } \mathbf{x} \in S_R \quad (3.2)$$

The normal stress jump across the liquid-liquid interface  $S_I$  is due to surface tension

$$\mathbf{n} \cdot [\sigma_1(\mathbf{x}) - \sigma_2(\mathbf{x})] = \gamma (\nabla_S \cdot \mathbf{n}) \mathbf{n} \text{ for } \mathbf{x} \in S_I \quad (3.3)$$

where  $\gamma$  is the interfacial tension and  $\nabla_S = (\mathbf{I} - \mathbf{nn}) \cdot \nabla$  is the gradient operator tangential to the surface, which, applied to the surface normal  $\mathbf{n}$ , yields two times the mean curvature of the interface  $2\kappa_m = (\nabla_S \cdot \mathbf{n})$ . Marangoni stresses are not considered in this model, the surface tension material parameter is assumed to be constant along the interface.

Along the interface  $S_I$ , we have the kinematic boundary condition

$$\frac{d\mathbf{x}}{dt} = \mathbf{u}(\mathbf{x}) \text{ for } x \in S_I \quad (3.4)$$

that is, the surface is advected along with the flow.

The flow field created by a sink positioned at  $\mathbf{x}_S$  is

$$\mathbf{u}_{\text{ext}}(\mathbf{x}) = \frac{Q}{4\pi|\mathbf{x}_S - \mathbf{x}|^3}(\mathbf{x}_S - \mathbf{x}) \quad (3.5)$$

In the experimental setup used by Cohen and Nagel, the capillary length in the system (Cohen & Nagel (2002)) was approximately 0.3 cm, much larger than the small-scale structure found near the transition (tip radius of the order of 100  $\mu m$ ). It is therefore believed that the main role of gravity is to set the boundary condition of an overall flat shape of the interface. Without an external flow, the interface will assume a flat horizontal shape (except for meniscus effects near the container walls) and is linearly stable against perturbations from this configuration.

In our setup, a similar role is played by the infinite reservoir pressure  $p_0$ .  $p_0$  selects the (linearly stable) interface shape when no external flow is present: a spherical cap of radius  $2/p_0$  (in non-dimensional units) cut off at the pinning radius  $a = 1$ . A completely flat interface corresponds to a reservoir pressure  $p_0 = 0$ .

To see how this boundary condition connects with the experiment, consider that in the experiment, the vanishing of the steady-state hump and subsequent entrainment of a spout is caused by viscous stresses overcoming surface tension at the tip of the hump. The radial extent of the hump is set by the smaller one of either the straw height or the capillary lengthscale. Away from this hump region, the interface assumes an almost flat shape, causing the flow to be nearly radial in direction. Therefore, viscous stresses should not contribute appreciably to the normal stress balance on the flat interface, which then is dominated by gravity. This makes the flat interface a surface of almost constant pressure.

For numerical reasons, it is simpler to work with a small but non-zero pressure. For most runs shown in this paper,  $p_0$  was chosen to be 0.01. A check against the  $p_0 = 0$  result showed that relative changes in the results (tip curvature, tip height, critical flow rate) are generally smaller than  $10^{-2}$ . The governing equations are non-dimensionalized by using the pinning radius  $a$  as the characteristic lengthscale and the viscous relaxation velocity  $\gamma/\mu$  as the characteristic velocity scale. With the characteristic timescale  $\mu a/\gamma$ , the nondimensional sink flow rate then is

$$Q = \frac{\mu Q/a^2}{\gamma}$$

A flow rate  $Q = O(1)$  corresponds to a sink at distance  $a$  that produces viscous stresses of the same order as surface tension stresses of a drop of radius  $a$ .

#### 4. Numerical formulation

Because solutions to the Stokes equation can be formulated in terms of Greens functions, we rewrite the governing equations as a system of integral equations over the

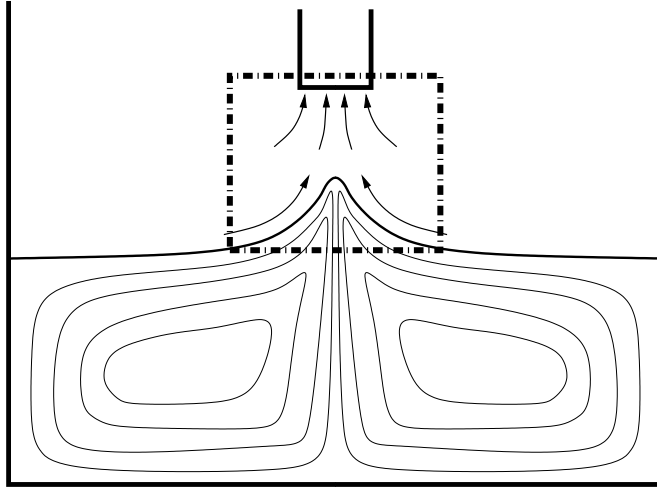


FIGURE 2. Schematic of the selective withdrawal experiment

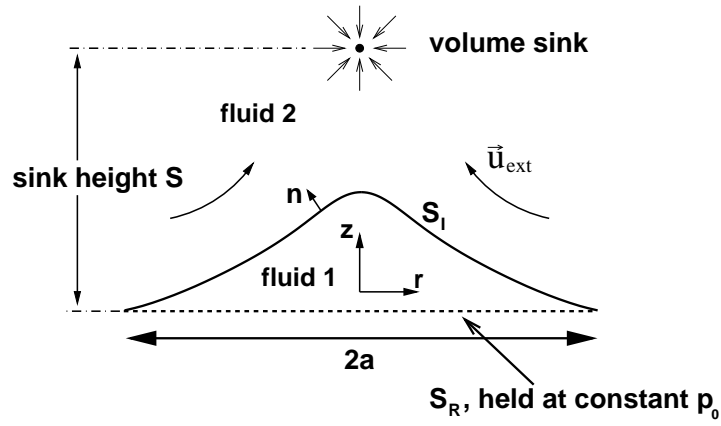


FIGURE 3. Simplified numerical model of selective withdrawal

boundaries using the boundary conditions mentioned above:  
on the interface  $S_I$  we have

$$\begin{aligned}
 \frac{1+\lambda}{2} \mathbf{u}(\mathbf{x}) &= \int_{S_I} \mathcal{J} \cdot \mathbf{n} [\gamma 2\kappa_m + \Delta \rho \mathbf{g} \cdot \mathbf{y}] dS_y & (4.1) \\
 &+ (1-\lambda) \int_{S_I} \mathbf{n} \cdot \mathcal{K} \cdot \mathbf{u} dS_y \\
 &+ \int_{S_R} \mathcal{J} \cdot \mathbf{n} p_0 dS_y + \lambda \int_{S_R} \mathbf{n} \cdot \mathcal{K} \cdot \mathbf{u} dS_y \\
 &+ \mathbf{u}_{\text{ext}}(\mathbf{x}) \text{ for } \mathbf{x} \in S_I
 \end{aligned}$$

whereas the flow on the reservoir surface is described by

$$\begin{aligned}
\frac{\lambda}{2} \mathbf{u}(\mathbf{x}) &= \int_{S_I} \mathcal{J} \cdot \mathbf{n} [\gamma 2\kappa_m + \Delta\rho\mathbf{g} \cdot \mathbf{y}] dS_y & (4.2) \\
&+ (1 - \lambda) \int_{S_I} \mathbf{n} \cdot \mathcal{K} \cdot \mathbf{u} dS_y \\
&+ \int_{S_R} \mathcal{J} \cdot \mathbf{n} p_0 dS_y + \lambda \int_{S_R} \mathbf{n} \cdot \mathcal{K} \cdot \mathbf{u} dS_y \\
&\text{for } \mathbf{x} \in S_R
\end{aligned}$$

with the tensors

$$\begin{aligned}
\mathcal{J}(\mathbf{r}) &= \frac{1}{8\pi} \left( \frac{\mathbf{1}}{r} + \frac{\mathbf{r}\mathbf{r}}{r^3} \right) & (4.3) \\
\mathcal{K}(\mathbf{r}) &= -\frac{3}{4\pi} \frac{\mathbf{r}\mathbf{r}\mathbf{r}}{r^5}
\end{aligned}$$

In this context, following the notation used in the experiment,  $\lambda$  is defined as the ratio of the viscosity of the lower fluid over that of the upper fluid:  $\lambda = \frac{\mu_1}{\mu_2}$ . In equation (4.1), the first term on the right hand side describes the flow contributions from surface tension forces along the liquid-liquid interface, whereas the second term accounts for different shear rates in the two liquids. This term vanishes when  $\lambda = 1$ . The third and fourth term contain the flow contributions from the (constant) normal stress forcing and the shear rates along the constant pressure reservoir surface, respectively. The last term incorporates the effects of the imposed outside flow.

In order to solve for the evolution of the liquid interfaces via the creeping flow equations, a C++ code has been set up that makes use of the boundary integral equations for STOKES flow in an axisymmetric setting. Because of the symmetry of the problem, all surfaces involved can be represented as effectively one-dimensional objects by their  $r$ - and  $z$ - coordinates in a cylindrical coordinate system. This allows for much greater resolution than a three-dimensional description at lower computational cost.

The liquid interface is parameterized by mesh points  $r_i(s_i), z_i(s_i)$ , where  $s_i$  denotes the arclength along the surface measured from the tip. The interface between mesh points is approximated by a cubic spline. This way, the curvature calculated for the LAPLACE pressure term varies continuously between mesh points. The distribution and number of points is adapted to the geometric shape of the surface. The algorithm we implemented chooses the density of points to be proportional to the mean curvature (in most runs  $\Delta s = 0.05/\kappa_m$ , where  $\Delta s$  is the arclength between two adjacent mesh points and  $\kappa_m$  is the mean curvature). Additionally, a maximum distance between mesh points cannot be exceeded. For most runs, this value was chosen to be of the order of 1/20 in dimensionless units. Since we start with an almost flat interface, this means that the initial shape is represented by 20 grid points. During a typical run, the number of mesh points on the interface is dynamically increased to about 60 in order to resolve a dimensionless tip curvature of approximately 75. An increase in the mesh resolutions shows no significant change in the results.

The constant pressure reservoir surface in the setup and the nozzle sidewalls (for the solid container runs) are represented by a uniform grid of points. The velocity (in the case of a constant pressure surface) and normal stress jump (in the case of a solid wall) between points are interpolated linearly. The constant pressure reservoir surface in the setup is represented by a mesh of 30 uniformly spaced points. The boundary integrals are evaluated using Gaussian quadratures. Singular parts of the integral are dealt with

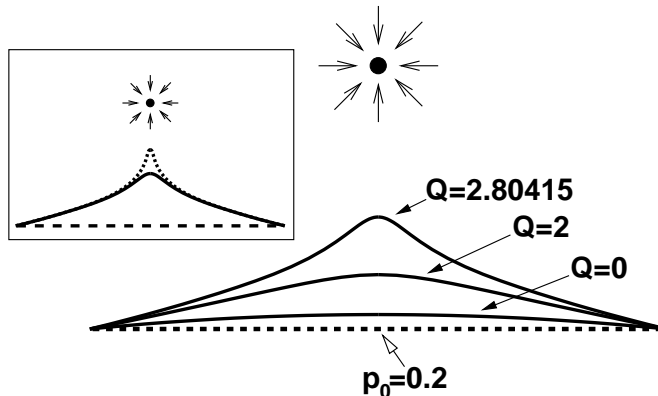


FIGURE 4. Sequence of surface shapes, run at  $p_0 = 0.2$ ,  $S = 1$ . The inset shows how the interface develops an instability near the tip for a flow rate above the threshold (dashed line).

separately using finer subdivisions of the integration interval, and the resulting algebraic equations for the unknown velocities and stresses are solved by LU (lower and upper triangular matrix) decomposition.

The azimuthal component of the boundary integral equations is integrated analytically, the resulting elliptic integrals evaluated numerically (see Lee & Leal (1982)).

The mesh points on the interface are advanced in time normal to the surface using explicit forward Euler timestepping. The length of each timestep is chosen proportional to the smallest mesh spacing. The validity of this approach was tested by doubling the time resolution for a given run and comparing to the original results. Generally, results obtained this way differed by less than 1%. We also experimented with an implicit backward Euler scheme, but the evaluation of the necessary Jacobian was prohibitively slow, and the results obtained by the two methods did not differ significantly. Furthermore, since we are evolving towards steady state configurations, details of the intermediate dynamics are only of secondary interest.

The scheme for finding steady state shapes and critical flow rates follows the experimental procedure: starting with a static configuration at zero flow rate,  $Q$  is increased in small steps and for each step the interface is allowed to relax into a steady state shape. Steady state is detected by observing that the modulus of the highest normal velocity on the interface,  $\mathbf{u}_{\max} \cdot \mathbf{n}$ , falls below a certain threshold ( $10^{-3}$  in dimensionless velocity units in most cases; lower thresholds were tested without significantly changing the results). When  $u_{\max}$  increases monotonically by a certain factor, we deduce that a steady-state hump shape has ceased to exist. In this case, the interval between the last steady state flow rate and the current flow rate is divided in half, creating nesting intervals containing the critical flow rate  $Q_c$ . This procedure is stopped when the interval size drops below the desired accuracy.

## 5. Dynamics near the transition

First, we analyze the sequence of steady-state shapes from a typical run, with particular focus on how geometric quantities characterizing the interface shape change near the threshold flow rate. Steady-state interface shapes at zero, moderate and threshold flow rates are shown in figure 4. The reservoir pressure is held at  $p_0 = 0.2$  and the sink is

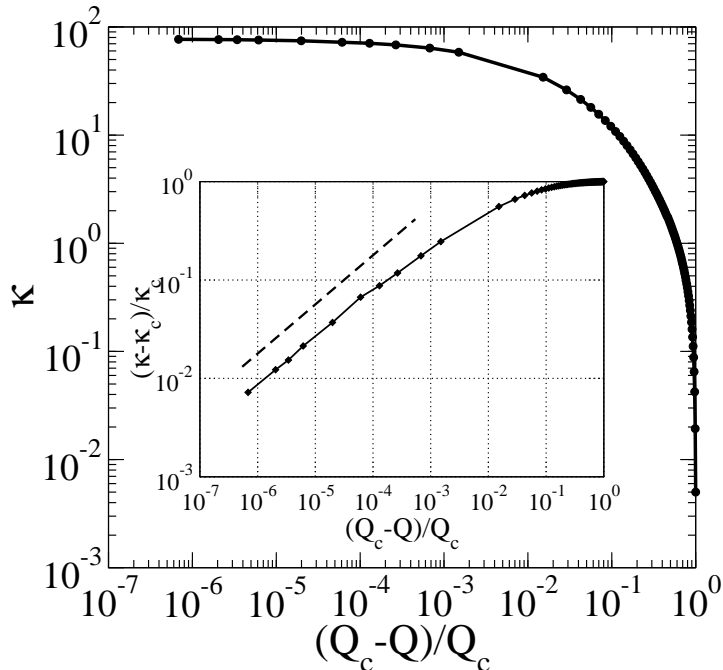


FIGURE 5. Curvature  $\kappa$  at hump tip versus  $Q_c - Q$ . The reservoir pressure is  $p_0 = 0.01$ , the sink height is  $S = 0.2$ . The inset shows  $(\kappa_c - \kappa)/\kappa_c$  as a function of  $(Q_c - Q)/Q_c$  in a log-log plot, with the dashed line depicting a square root powerlaw.

located at distance 1 above the reservoir †. The  $Q = 0$  interface is a spherical cap with its curvature determined by the reservoir pressure. At  $Q = 2$ , a broad hump develops on the interface. The volume between the backsurface and the interface has increased significantly. At the entrainment threshold ( $Q = 2.80415$ ), the interface forms a distinct hump directly below the sink, which broadens away from the sink to smoothly join onto the pinned edge. Just above the entrainment threshold, at  $Q = 2.80416$ , no steady-state hump exists. Instead, the tip of the hump sharpens and extends towards the sink over time (inset of figure 4). Notice that while the steady-state hump radius can be much smaller than the pinning radius, it remains comparable to the hump height. Changing the pressure  $p_0$  on the reservoir surface from  $-0.3$  to  $0.5$  changes the values of the hump height or tip curvature at all flow rates by at most a few percent. Changing the sink height  $S$  does change both lengthscales significantly, however, as will be shown later, it does not qualitatively change the features of the interface evolution described above. Figure 5 illustrates the evolution of the mean curvature  $\kappa$  at the hump tip as a function of  $(Q_c - Q)/Q_c$  for a typical run with  $p_0 = 0.01$  and  $S = 0.2$ . The tip curvature clearly saturates as  $Q_c$  is approached. The range of possible values for  $Q_c$  is strongly limited by our interval bisection method used to find steady-state shapes ‡. The inset shows that

† A relatively high reservoir pressure  $p_0 = 0.2$  is chosen here to make the initial interface shape more visible

‡ The value  $Q_c$  must lie between the largest  $Q$  that still gives rise to a steady-state hump and the smallest  $Q$  which, starting from a lower flow rate, results in a spout being entrained into the sink. We can use the size of this last interval as a rough estimate for the expected error in  $Q_c$ . With the prefactor of the  $1/2$ -powerlaw we can then propagate the estimated error in  $Q_c$  to  $h_c$  and compare this to the values of  $h_c$  from the fit and the value of  $h$  for the last stable steady-state found numerically. These values are found to be consistent with each other.

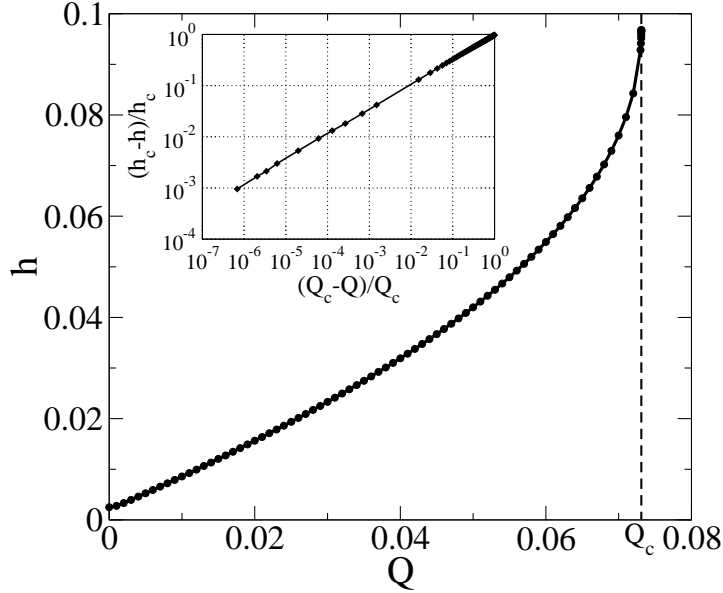


FIGURE 6. Steady-state hump height  $h$  versus sink flow rate  $Q$ . The reservoir pressure for this run is  $p_0 = 0.01$ , the sink height above the reservoir interface is  $S = 0.2$ . The inset shows  $(h_c - h)/h_c$  as a function of  $(Q_c - Q)/Q_c$  in a log-log plot.

the tip curvature  $\kappa$  approaches its saturation value  $\kappa_c$  as a square root of  $(Q_c - Q)/Q_c$ . Notice that the square-root scaling becomes evident only when  $(Q_c - Q)/Q_c$  is less than roughly  $10^{-3}$ . In figure 6 the height  $h$  of the hump over the constant pressure reservoir surface in steady-state for different flow rates  $Q$  is shown. The hump height  $h$  approaches its saturation value  $h_c$  along a half-parabola as the flow rate  $Q$  approaches the threshold value  $Q_c$ . The same value of  $Q_c$  was used to analyze the evolutions of  $\kappa$  and  $h$ . The inset shows that  $(h_c - h)/h_c$  also scales as a square root of  $(Q_c - Q)/Q_c$ . We therefore conclude that the steady-state hump vanishes via a saddle-node bifurcation, consistent with results from emulsification studies.

To get a more detailed view of how the shape evolves near  $Q_c$ , we analyze the behavior of the interface half-width and half-height near their threshold values. The difference between the half-width  $r(z = h_{\max}/2)$  and its threshold value again scales as  $\sqrt{(Q_c - Q)/Q_c}$  (see figure 7), whereas the half-height  $h(r = 1/2)$  approaches its threshold value almost linearly in  $(Q_c - Q)/Q_c$ . Only near the tip region, that is  $h(r)$  for  $r < 1/\kappa$ , does the hump height exhibit square root scaling. This dependence indicates that the dominant mode of surface deformation that becomes unstable at the threshold flow rate and undergoes a saddle-node bifurcation corresponds to a mostly radial adjustment of the entire shape and an axial adjustment in the tip region.

While a saddle-node bifurcation is a generic transition for shape change, we can understand why it occurs in selective withdrawal by considering how shape perturbations on the steady-state interface interact with the imposed withdrawing flow. First, notice that the imposed withdrawal flow due to the point sink always speeds up towards the sink and away from the interface. This suggests that, for a flow rate  $Q$  below  $Q_c$ , there exist two possible steady-state solutions, one stable and one unstable. To see this, consider what happens when we perturb the shape of the stable steady-state interface. Clearly the most destabilizing shape perturbation is one that pulls the tip of the hump towards the sink. If the amplitude of such a shape perturbation is small, we expect the hump will simply

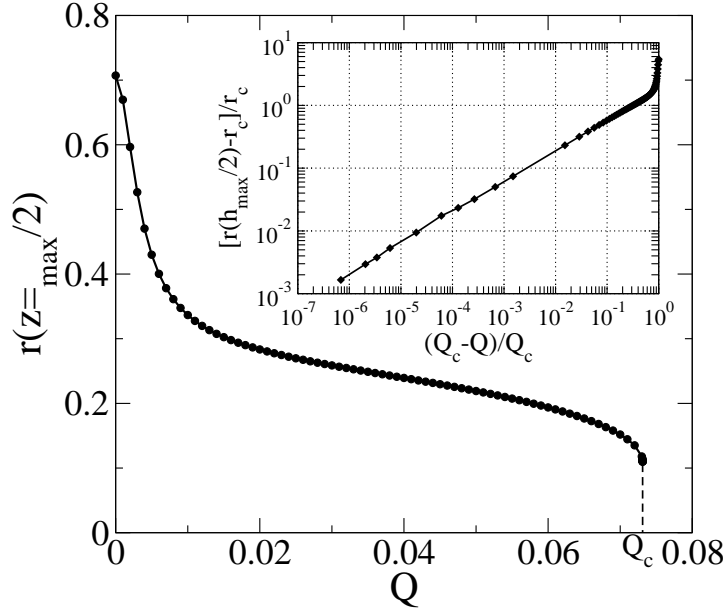


FIGURE 7. Half-width  $r(h_{\max}/2)$  versus sink flow rate  $Q$ . The reservoir pressure is  $p = 0.01$ , the sink height is  $S = 0.2$ . The inset shows  $r(h_{\max}/2) - r_c$  as a function of  $Q_c - Q$  in a log-log plot.

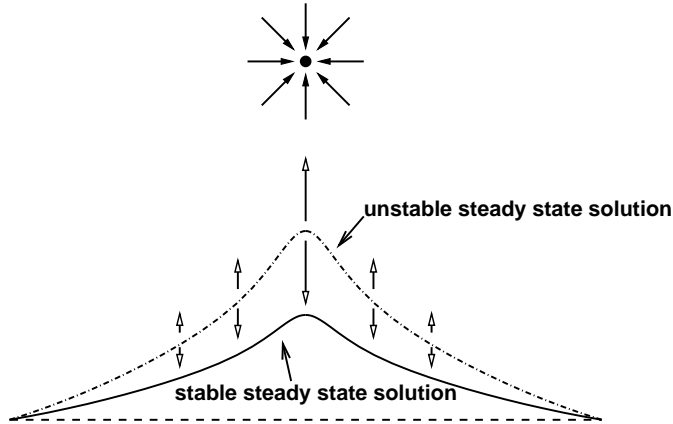


FIGURE 8. Saddle-node bifurcation in the selective withdrawal system

relax back to its original height. If the amplitude is sufficiently large, we expect the perturbation to initially grow, so that the hump is drawn up into the sink. While it is unclear what happens to the interface with a true singularity in the flow (such as our point sink), in the experimental situation of withdrawal through a pipette, no appreciable hysteresis was observed between the hump-to-spout transition and the spout-to-hump transition. Therefore, the perturbed interface cannot evolve into a steady-state spout. It will be withdrawn briefly, then break apart due to surface tension effects and relax back to the original shape. These two different outcomes suggest there exists a critical shape perturbation which neither decays nor grows, and therefore constitutes an unstable steady-state shape. As illustrated in figure 8, the unstable steady-state shape essentially divides interface profiles which grow towards the sink from profiles which directly decay towards the stable shape. When  $Q$  approaches  $Q_c$ , the amplitude of the perturbation needed to

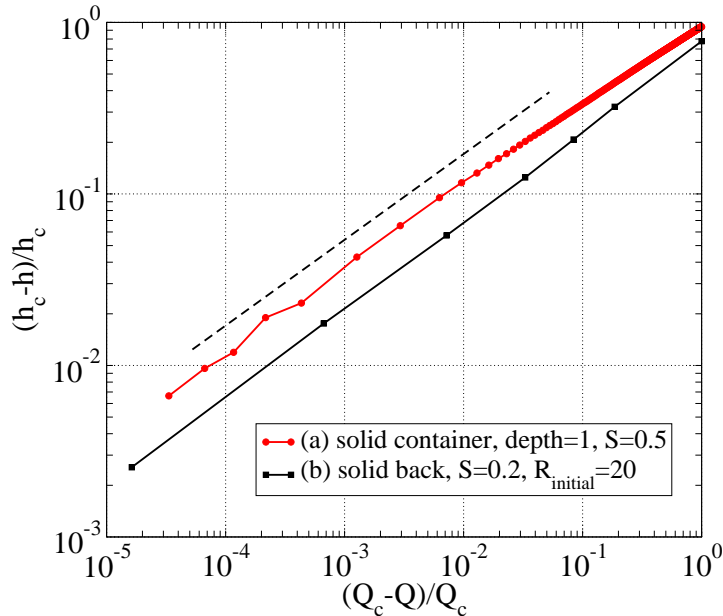


FIGURE 9. Scaling of hump height  $h$  near the transition flow rate for two different sets of boundary conditions. The dashed line indicates a square root powerlaw.

cause the interface to grow towards the sink decreases. Equivalently, the unstable and stable steady-state hump solutions approach each other. At  $Q_c$ , the unstable and stable solutions coincide and annihilate.

The mechanism outlined here requires only that a steady-state interface exists and that the imposed flow speeds up away from the interface. Both requirements are satisfied in the case of drop emulsification in a straining flow, and a saddle-node bifurcation is observed there. We also expect the generic shape transition for the steady shape in selective withdrawal is a saddle-node bifurcation when different boundary conditions are imposed or when the two fluid layers have different viscosities. Figure 9 presents the scaling analysis for the hump height with different boundary conditions. Set (a) corresponds to withdrawal from a cylindrical container. Set (b) corresponds to withdrawal from a thin lower layer which is resting on a solid plate. Both runs yield results that are in good agreement with the expected scaling near a saddle-node bifurcation. In addition, we have repeated this analysis for various runs with different sink heights, back pressures and types of backsurfaces, and find that the hump always disappears via a saddle-node bifurcation. We also find that the tip curvature always saturates upon approach to the threshold flow rate, consistent with a saddle-node bifurcation.

This contradicts the interpretation by Cohen and Nagel in (Cohen & Nagel (2002)), that  $(h_c - h)/h_c \propto ((Q_c - Q)/Q)^{0.64}$  and  $\kappa \propto ((Q_c - Q)/Q)^{-0.75}$ . Therefore, we compare our results with the unscaled experimental data from viscous selective withdrawal with a water-glycerin mixture as the lower and heavy mineral oil as the upper liquid. The viscosity ratio of the system is  $\lambda \approx 0.83$ . This is reasonably close to the viscosity ratio of  $\lambda = 1$  used in our model calculations to allow for a comparison of the two systems.

Figure 10 shows a plot of the rescaled steady-state hump-heights  $(h_c - h)/h_c$  versus the rescaled, imposed flow-rates  $(Q_c - Q)/Q_c$  for various experimental runs as well as the numerical equivalent already presented in figure 6. The measurement errors are comparable with the symbol size. The dashed line shows a square root power law for

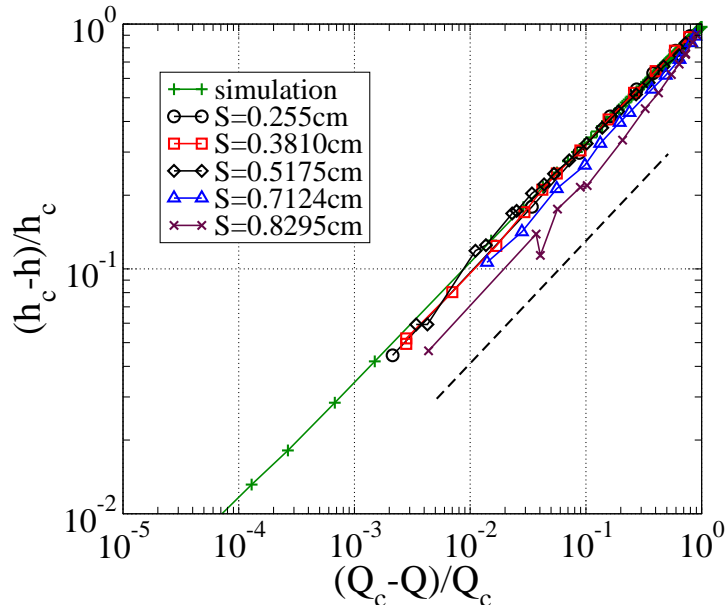


FIGURE 10. Rescaled hump heights  $(h_c - h)/h_c$  versus rescaled flow rates  $(Q_c - Q)/Q_c$  for the experimental data.

reference. For all the experimental runs, we find that good agreement with the square root scaling is produced by slightly adjusting the threshold values reported by Cohen and Nagel, typically by around 5%. Notice that the range in  $(Q_c - Q)/Q_c$  of the numerical data is considerably larger than that of the experiment. We conclude that the measured evolution of the hump heights is consistent with a saddle-node bifurcation near the transition.

Next we re-examine whether the measured tip curvature diverges near the transition. In order to compare the experimental measurements and the numerical results, we rescale the tip curvature by the threshold hump height  $h_c$ . We plot the rescaled tip curvature versus the rescaled flow rate for various experimental runs as well as our numerical data in figure 11. The  $Q_c$  values obtained from the scaling analysis of the hump height are used (see figure 10). The graph shows that the experimental data falls on top of the numerical results, even though the curvature is still approaching its saturation value. The good agreement strongly suggests that the tip curvature in the experiment is consistent with a saddle-node bifurcation. A fuller discussion of how the restricted range in the experimental measurements allows both interpretations can be found in Appendix A.

## 6. Dynamics over the entire range of flow rates

So far, we have explored the evolution of the interface near the threshold flow rate  $Q_c$ . It is also worthwhile to examine how the steady-state shape evolves from a nearly flat interface into a highly curved hump as the withdrawal flow rate  $Q$  increases. We show below that the hump height and the tip curvature remain coupled for all flow rates. Surprisingly, the coupling is strongly asymmetric: the tip curvature increases dramatically while the hump height remains roughly constant. Changing the boundary conditions on the interface does not lead to qualitative changes in the coupling between the two lengthscales.

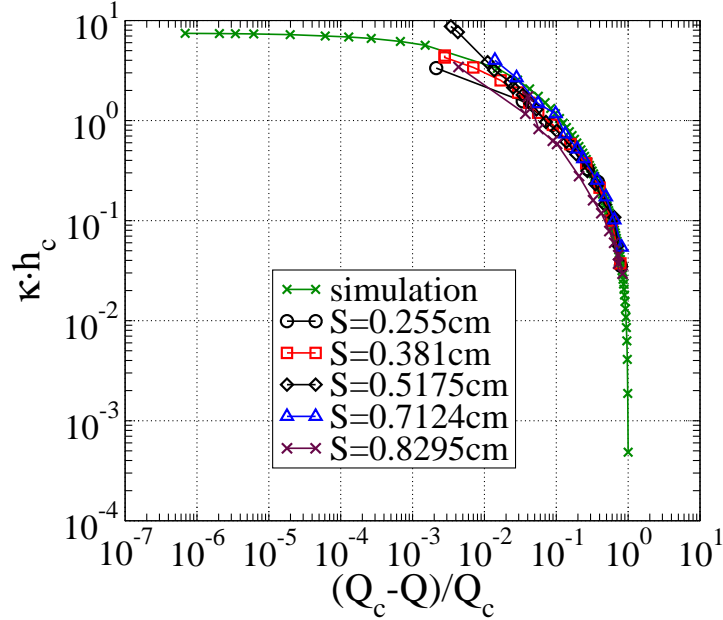


FIGURE 11. Tip curvature versus rescaled flow rate  $(Q_c - Q)/Q_c$  for the numerical model and experimental data. The tip curvature has been non-dimensionalized using the threshold hump height  $h_c$ . The model system parameters are  $S = 0.2$ ,  $p_0 = 0.01$ .

In figure 12, the dependence of the steady-state tip curvature  $\kappa$  on the hump height  $h$  is illustrated in a semi-log plot. Both quantities are non-dimensionalized using the threshold hump height  $h_c$ . Each point corresponds to a steady-state interface shape for a given flow rate  $Q$ . For small  $Q$ , and hence small  $h$ , the tip curvature increases very quickly with the hump height. This steep rise is then followed by an almost exponential dependence of  $\kappa$  on  $h$ . Although the tip radius  $1/\kappa$  is much larger than the hump height  $h$  at low flow rates, the rapid increase of  $\kappa$  relative to  $h$  causes the tip radius to be comparable with the hump height at the entrainment threshold. For the constant pressure run displayed in figure 12, the separation of the two lengthscales at the entrainment threshold,  $h_c \cdot \kappa_c = h_c/R_{\text{tip}}$ , can be read off the right-most point in the graph and is approximately 7. The strong, almost exponential, dependence of the tip curvature on the hump height is surprising, since the velocity field near the hump tip varies smoothly with distance from the tip, and remains unexplained.

In our numerical model, three lengthscales are introduced by the boundary conditions: the sink height  $S$ , the pinning radius  $a$  and the radius of curvature at the pinning edge, given by  $2/p_0$ . In addition, one can define a viscous length  $\ell_\mu = (\gamma S^3)/(\mu Q)$  by balancing surface tension effects and viscous stresses. Given this plethora of lengthscales, it is unclear which one is relevant for the hump shape. In particular, it is unclear which lengthscale, if any, will shift the separation of lengthscale  $h_c \cdot \kappa_c$  at transition. To answer this question, we first changed the pressure of the infinite reservoir from  $p_0 = -0.3$  to  $p_0 = 0.5$ . This did not change the hump shape significantly and therefore resulted in no significant change of  $h_c \cdot \kappa_c$ . We then examine the role of the sink height  $S$ . Figure 13 shows how the curvature  $\kappa_c$  and the hump height  $h_c$  at threshold flow rate change with  $S$ . The dashed lines indicate a reciprocal and linear relationship, respectively. In the limit of  $S \gg a$ ,  $\kappa_{\text{max}}$  and  $h_{\text{max}}$  appear to saturate to asymptotic values. This is due to the fact that for large  $S$ , the flow at the interface is almost uniform on the scale of the pinning

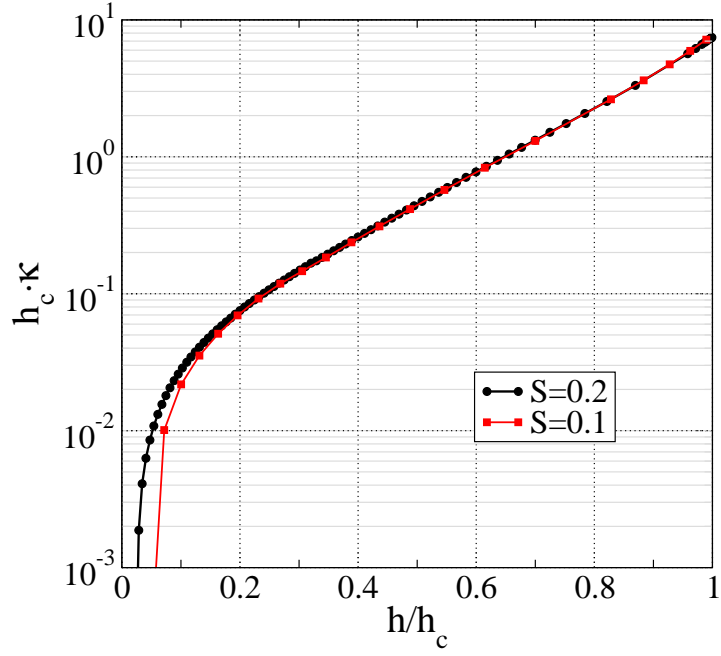


FIGURE 12. Tip curvature  $\kappa$  at threshold flow rate for different sink heights  $h_c$ .

$S = 0.2$ . The hump height  $h_c$ .

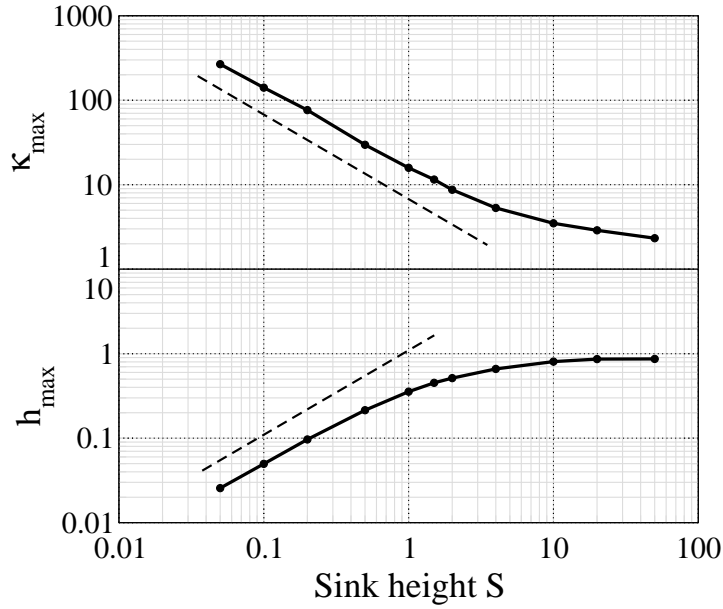


FIGURE 13. Tip curvature  $\kappa_{\max}$  and hump height  $h_{\max}$  at threshold flow rate for different sink heights  $S$ . The dashed line corresponds to a linear relation.

radius  $a$ . In the other limit of  $S \ll a$ , the tip radius  $1/\kappa$  and the hump height become proportional to the sink height. This is indicative of the fact that in this limit the sink height  $S$  becomes the only relevant lengthscale in the system, and the effects of holding the interface pinned at radius  $a$  vanish. By rescaling all lengths in the system by the sink

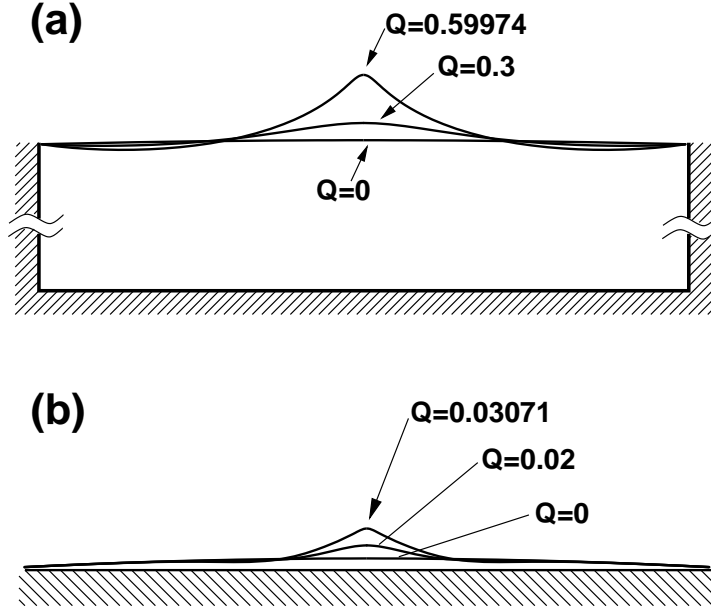


FIGURE 14. (a) setup with no-slip instead of constant pressure boundary condition; (b) setup with container with solid walls

height  $S$ , the dependence of the hump height and tip curvature vanish trivially in this case. Consequently,  $\kappa_c \cdot h_c$  stays fixed at a value of roughly 7 for  $S < a$ . The absence of a  $S^3$  scaling over the entire range of  $S/a$  also rules out any possible dependence on  $\ell_\mu$ .

Since  $h_c \cdot \kappa_c$  remains roughly constant for all possible realizations of the simplified numerical model, we next consider more drastic changes in the boundary conditions. Figure 14 gives two specific realizations. Part (a) shows a setup in which a container with solid walls holding the bottom fluid is simulated. Part (b) shows a setup in which the constant pressure reservoir surface is replaced by a no-slip surface. This corresponds to a drop on a solid plate, with its edges pinned at radius  $a$ . The initial volume of fluid for the solid backsurface run was given by a spherical cap of radius 20 and the sink was placed at  $S = 0.2$ . For the solid container, the sink was placed at a height  $S = 0.5$  above the interface. For the interface pinned atop the container (part a), we start out with a flat interface. The interface develops into a distinctive hump below the sink at threshold flow rate. Because the interface is held fixed at the edge and since volume is conserved in this setup, the shape shows a small dip below the neutral level between the hump and the pinning edge. This dip compensates for the volume of fluid forming the hump. In the case of the interface pinned on a solid plate, the shape evolves into a hump containing the bulk of the fluid centered under the sink. The base of the hump spans roughly half of the pinning radius. Since volume is conserved and the interface is pinned at the edge, this results in an almost flat interface between the pinning site and the cone base. Despite major changes to the reservoir condition, the typical sequences of surface shapes at zero, intermediate and threshold flow rates are very similar to the shapes for the constant-pressure run (figure 4).

More specifically, the separation of lengthscales  $h_c \cdot \kappa_c$  for the container run is approximately 7, while the solid back surface run gives  $h_c \cdot \kappa_c \approx 4$ . We have considered other variations, both in the boundary conditions and in the imposed flow. None of these led to significant changes in  $h_c \cdot \kappa_c$ . Figure 15 includes six sets of data. Three sets corre-

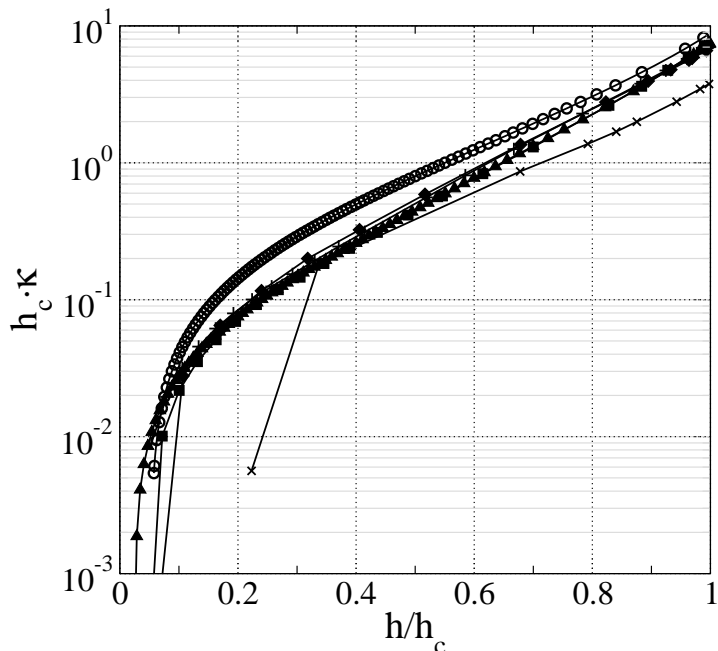


FIGURE 15. Tip curvature  $\kappa$  versus hump height  $h$  for runs of the simulation with various boundary conditions. The curvature and the hump height are non-dimensionalized by the threshold hump height  $h_c$ . Three sets correspond to  $p_0 = 0.01$  but with the sink height at  $S = 0.1$  (solid squares) and  $S = 0.2$  with (solid triangles) and without gravity (capillary lengthscale  $l_c = 0.1$ , plus signs). Open circles correspond to a run with the sink at  $S = 0.5$  and a container instead of the backsurface. Solid diamonds denote a run where the flow in the upper fluid is driven by a sink with a vortex ring around it, the latter imitating the effects of the flow passing the opening of the withdrawing straw. The final set has the sink height at  $S = 0.2$ , but replaces the constant pressure backsurface by a solid plate (X).

spond to  $p_0 = 0.01$  but with the sink height at  $S = 0.1$  (solid squares) and  $S = 0.2$  with (solid triangles) and without gravity (plus signs). Open circles correspond to a run with the sink at  $S = 0.5$  and a solid-walled, fluid filled container instead of the backsurface. Solid diamonds denote a run where the flow in the upper fluid is driven by a vortex ring and a sink. The final set has the sink height at  $S = 0.2$ , but replaces the constant pressure backsurface by a solid plate (X). Remarkably all these different runs show a strong, approximately exponential dependence. Although the interface shape, in particular the actual values of the tip curvature and hump height, varied significantly among these different runs, the different curves collapse almost entirely when  $h$  and  $\kappa$  are rescaled by the threshold hump height  $h_c$ . Only the solid plate run produces a curve with a distinctively smaller slope.

Finally, we re-plot the experimental data to see whether the same scenario obtains when the measured  $h$  and  $\kappa$  are rescaled by  $h_c$ . Again, the curves roughly collapse onto one curve, except for  $S = 0.8295\text{cm}$ , as shown in figure 16. As  $S$  increases, the experimental curves show a more and more pronounced upturn near  $h_c$ . Probable mechanisms for this discrepancy are inertia of flow in the upper fluid, or the interface away from the hump dipping below the  $Q = 0$  level due to mass conservation or viscous stresses from the flow. Both effects should become more pronounced as  $S$  increases. A similar, though smaller amplitude optic, is observed in our simulation of selective withdrawal from a container. In that case, the optic can be directly related to the dipping of the interface. Consistent

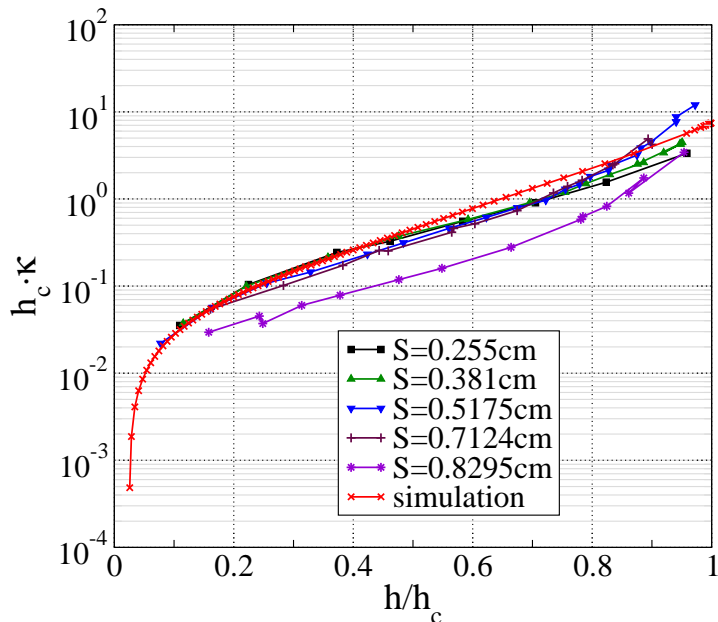


FIGURE 16. Tip curvature  $\kappa$  versus hump height  $h$  for the numerical model and experimental data. Both quantities have been non-dimensionalized using the threshold hump height  $h_c$ .

with the simulation, the separation of lengthscales  $h_c \cdot \kappa$  in the experiments varies from 5 to 14. Again, the two lengthscales are comparable. If one defines an equivalent ratio for equal viscosity drop breakup by using the tip curvature versus the half-length of the drop, one finds a value of 3. Thus the numerical model produces a separation of lengthscales that is only about a factor 2 larger than in the drop breakup case. Clearly, this difference is small enough to be attributed to the change in overall geometry between the two situations. In addition, the collapsed experimental curve lies close to the numerical curve for constant pressure. This agreement is not surprising, since numerical solutions for very different reservoir conditions roughly collapse onto a single curve. For two layers of equal viscosity,  $h_c \cdot \kappa$  appears to have always the same relation with  $h/h_c$ . This suggests the steady-state velocity fields and profiles observed under these different conditions are roughly geometrically similar.

## 7. Discussion

Here we describe a number of different studies that could naturally complement this one and comment on the relevance of our results for topological transitions in steady-state interfaces in general. In analyzing how the steady-state hump disappears near the threshold, we have proposed a simple physical mechanism that accounts for why the hump solution vanishes via a saddle-node bifurcation. In this picture, an unstable steady-state shape acts as a boundary dividing shape perturbations that decay monotonically from those that grow initially. As a result, even though an unstable shape cannot be observed in the experiment, its existence has consequences on the transient dynamics. Simulations using Newton-relaxation techniques could obtain unstable shapes, and thereby assess their influence. Also, the proposed mechanism requires that the withdrawal flow speeds up away from the interface. This suggests the deformation and burst of an interface in

a uniform external flow may have very different characteristics than those observed in selective withdrawal.

The selective withdrawal experiment has shown that above the transition, entrained spouts are produced instead of steady-state humps. The steady-state entrained spout can be used to encapsulate particles and biological cells (Wyman *et al.* (2004); Cohen *et al.* (2001)), or be solidified into thin fibers. By characterizing the possible hump shapes at transition, our study gives indirect information about the thinnest steady-state spout obtainable. Experimental characterization of the spout shape is difficult because the spout shape changes everywhere as the imposed flow rate changes so that, without information about the velocity field inside the spout, it is not possible to compare results under different conditions systematically. It is therefore worthwhile to extend the numerical model so that the spout-formation dynamics can be simulated directly. One possibility is to use a vortex-ring, instead of a point sink, to generate the withdrawing flow, and using a suitable boundary condition at the downstream end of the spout.

The  $\mu_0 = \mu$  simulation here suggests that  $h_c \cdot \kappa_c$ , the separation of lengthscales at the entrainment threshold, has a weak dependence on the boundary conditions and the type of imposed flow. In contrast, a long-wavelength analysis of steady-state spout shapes with  $\mu_0 \ll \mu$  shows the minimum spout size depends strongly on boundary conditions (Zhang (2004)). It may be possible that for unequal viscosities, the boundary conditions can exert a much stronger effect on the steady-state interface shape, and possibly result in steady-state hump shapes with tip radii far smaller than the hump height. The existing evidence are conflicting. Experiments on selective withdrawal (Cohen & Nagel (2002); Cohen (2004); Case & Nagel (2005)) report threshold shapes with essentially the same separation of lengthscales, regardless of the viscosity contrast. In drop emulsification, steady-state drop shapes depend strongly on  $\lambda$ . While long and slender drops with highly curved tips are produced in the limit  $\lambda \ll 1$ , only slight distortions from a sphere in the steady-state shape of the drop can be sustained when  $\lambda \gg 1$ . Air entrainment studies which analyze 2D shape transitions in two fluid layers show that, when  $\mu_0 = 0$ , the steady-state interface approaches a singular shape as the flow rate increases (Joseph *et al.* (1991); Jeong & Moffatt (1992); Lorenceau *et al.* (2003)). When  $\mu_0 \ll \mu$ , the approach to the singular shape is cut off at a small lengthscales which is a fraction of the tip height, with the fraction scaling as  $\lambda^{4/3}$  (Eggers (2001); Lorenceau *et al.* (2003)). There is a clear need for accurate numerical analysis of the selective withdrawal transition with different layer viscosities.

We next consider to what extent the results obtained here are of relevance to drop production in microfluidic devices, and to surfactant- or electric field-driven shape transitions. In microfluid channel devices that use "flow-focusing" or geometric constraints to generate liquid drops, the interfaces forming these drops are subjected to viscous and surface tension effects and similar pinning boundary conditions and reservoir conditions. Therefore the results are directly relevant, and suggest that, when the drop viscosity is comparable with the surrounding liquid viscosity, the drop formation dynamics are robust. Changing the boundary conditions or flow conditions will only lead to minor changes in the drop size. However, if surfactants are present, we expect the focusing of the flow at the hump tip to cause surfactant to accumulate at the tip and therefore lead to the creation of droplets much smaller than the channel dimension (De Bruijn (1993); Eggleton *et al.* (2001); Fernandez & Homsy (2003, 2004); Krechetnikov & Homsy (2004)). A similar shape transition occurs in tip streaming, in which initially dilute amounts of surfactants accumulate at the extended tip of a drop in a straining flow and lead to ejection of very small drops. In some sense, the creation of drops whose size is far smaller than the characteristic lengthscales of the boundary results from the fact that a

second nonlinear coupling is in effect. The interface is nonlinearly coupled to the surfactant distribution, as well as to the flow. In addition, the hump-to-spout transition also resembles the Taylor cone-jet transition when a liquid interface separating a perfect conductor and air is deformed by an electric field (Taylor (1964*b*); Li *et al.* (1994); Zubarev (2002); Reznik *et al.* (2004)). Since the stream function for axisymmetric viscous flow satisfies the biharmonic equation, while the potential for the electric field satisfies Laplace's equation, the similar mathematical structure of the governing equations suggests that the resultant dynamics would also be similar. However, the analogy is complicated by the fact that the deformed interface shape below the threshold strength of the applied electric or magnetic field correspond to a static structure, so that the shape transition involves a change from a closed interface to an open interface whose shape is determined by flow effects. Therefore the topological transition corresponds to a change in the physical processes that determine the surface shape. This brief comparison suggests an obvious way to order these visually similar shape transitions in terms of increasing complexity. The simplest example corresponds to selective withdrawal with two layers of equal viscosities, in which the interface shape is determined by one nonlinear interaction, the interaction of the viscous flow in the two layers with surface tension effects. At the next level of complexity is withdrawal from two layers of extremely dissimilar viscosities, or equal-viscosity withdrawal with surfactant effects. In all these situations, the same physical effects are present before and after the transition. But the interface shape is determined by two nonlinear interactions: the coupling of the flow with the interface, and the coupling of the two dissimilar velocity fields (or the flow field and the surfactant concentration field). The formation of Taylor cones corresponds to the most subtle example, since the physical effects determining the interface shape change across the shape transition.

## 8. Conclusions

In this study, we constructed a simplified numerical model of the selective withdrawal experiment for two fluids of equal viscosity. We find that steady-state humps exist up to a threshold sink flow rate  $Q_c$ . Above this threshold, no steady-state surface shapes are found, the interface is drawn into the sink instead. We analyze how the interface approaches its critical shape near the transition and find that the system goes through a saddle-node bifurcation. We were able to compare our numerical results to experimental data in a similar parameter regime and find that the two sets are consistent with each other. The experimental data can also be interpreted in the context of a saddle-node bifurcation with saturating tip curvature. We find that  $(h_c - h)/h_c$  shows square root scaling in  $(Q_c - Q)/Q_c$  over the entire range of  $Q$  values, while  $(\kappa_c - \kappa)/\kappa_c$  exhibits this behavior only closer to  $Q_c$ . Therefore, the saturation of  $h$  is more easily observable than the saturation of  $\kappa$ . The larger dynamic range in  $Q$  close to the transition in the numerics allows us to identify the nature of the transition more clearly than the experiment. We also examined how the steady-state interface evolves as  $Q$  increases under different reservoir conditions. Numerics and experiments show that, for two layers of equal viscosity, the rescaled tip curvature  $h_c \cdot \kappa$  appears to have always the same relation with the rescaled hump height  $h/h_c$ . This suggests the steady-state velocity fields and profiles observed under these different conditions are roughly geometrically similar. As a consequence, the hump can never become very sharp relative to its height for equal viscosity layers.

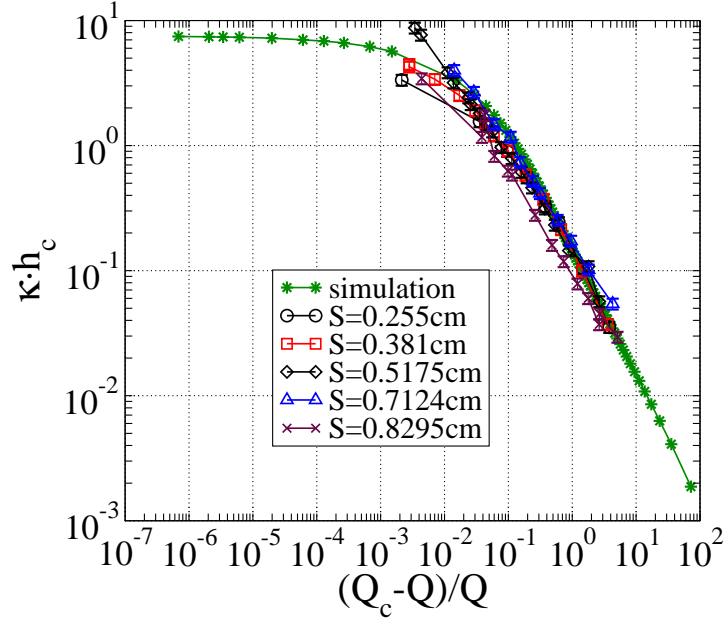


FIGURE 17. Tip curvature versus rescaled flow rate  $(Q_c - Q)/Q$  for the numerical model and experimental data. The tip curvature has been non-dimensionalized using the threshold hump height  $h_c$ . Errors in the experimental tip curvature were estimated to be approximately 10%. The model system parameters are  $S = 0.2$ ,  $p_0 = 0.01$ .

## Acknowledgements

We thank Sidney R. Nagel and Sarah Case for encouragement and helpful discussions. We also acknowledge helpful conversations with Francois Blanchette, Todd F. Dupont, Alfonso Ganan-Calvo, Leo P. Kadanoff, Robert D. Schroll, Howard A. Stone, Thomas P. Witelski, Thomas A. Witten and Jason Wyman. This research was supported by the National Science Foundation's Division of Materials Research, the University of Chicago Materials Lab (MRSEC), and by the DOE-supported ASC / Alliance Center for Astrophysical Thermonuclear Flashes at the University of Chicago.

## Appendix A.

As was seen in previous sections, compared to the hump height, the tip curvature shows evidence of saturation towards a final value only when  $Q$  is very close to  $Q_c$ . As a consequence, when the entrainment threshold is approached, the tip curvature can appear to diverge while the hump height reaches a saturation value. In particular, when  $\kappa$  is plotted against  $(Q_c - Q)/Q$  instead of  $(Q_c - Q)/Q_c$ , it is very difficult to distinguish between a continued power law and a turn over into saturation with the available range of experimental data. This is because even a slight shift in the value of  $Q_c$  can straighten out the curves. The powerlaw behavior in the  $(Q_c - Q)/Q$  range between 1 and  $10^{-2}$  seems to be mainly caused by the fact that in this range, the denominator of  $(Q_c - Q)/Q$  is always close to  $Q_c$  and almost constant, thus the entire expression scales roughly like  $1/Q$ . Furthermore, for small flow rates  $Q$  the system response to the outside flow can be assumed to be almost linear, with a linear dependence of  $\kappa$  on  $Q$ . This would then asymptotically give rise to a powerlaw with an exponent of  $-1$ .

## REFERENCES

- ACRIVOS, A. & LO, T. S. 1978 Deformation and breakup of a single slender drop in an extensional flow. *J. Fluid Mech.* **86** (4), 641–672.
- BARENBLATT, G. I. 1996 *Scaling, self-similarity and intermediate asymptotics*. Cambridge, UK: Cambridge University Press.
- BLAWZDZIEWICZ, J., CRISTINI, V. & LOEWENBERG, M. 2002 Critical behavior of drops in linear flows. i. phenomenological theory for drop dynamics near critical stationary states. *Physics of Fluids* **14** (8), 2709–2718.
- BOHR, N. 1939 Disintegration of heavy nuclei. *Nature* **143**, 330–331.
- BUCKMASTER, J. D. 1973 The bursting of pointed drops in slow viscous flow. *J. Appl. Mech.* **E 40**, 18–24.
- CASE, S. & NAGEL, S. R. 2005 Selective withdrawal with an inverted viscosity ratio. APS March Meeting, H37.008.
- CASNER, A. & DELVILLE, J. P. 2001 Giant deformations of a liquid-liquid interface induced by the optical radiation pressure. *Phys. Rev. Lett.* **87**, 054503.
- CHANDRASEKAR, S. 1967 *An Introduction to the Study of Stellar Structure*. New York: Dover.
- CHEN, D. L., GERDTS, C. J. & ISMAGILOV, R. F. 2005 Using microfluidics to observe the effects of mixing on nucleation of protein crystals. *J. Am. Chem. Soc.* **127**, 9672–9673.
- CHEN, Y. J. & STEEN, P. H. 1997 Dynamics of inviscid capillary breakup: Collapse and pinch-off of a film bridge. *J. Fluid Mech.* **341**, 245–267.
- COHEN, I. 2001 Scaling dependence on the fluid viscosity ratio in the selective withdrawal transition. PhD thesis, The University of Chicago.
- COHEN, I. 2004 Scaling and transition structure dependence on the fluid viscosity ratio in the selective withdrawal transition. *Phys. Rev. E* **70**, 026302.
- COHEN, I., BRENNER, M. P., EGGERS, J. & NAGEL, S. R. 1999 Two fluid drop snap-off problem: Experiments and theory. *Phys. Rev. Lett.* **83**, 1147–1150.
- COHEN, I., LI, H., HOUGLAND, J. L., MRKSICH, M. & NAGEL, S. R. 2001 Using selective withdrawal to coat microparticles. *Science* **292**, 265–267.
- COHEN, I. & NAGEL, S. 2002 Scaling at the selective withdrawal transition through a tube suspended above the fluid surface. *Phys. Rev. Lett.* **88** (7), 074501.
- CRISTINI, V. & TAN, Y. C. 2004 Theory and numerical simulation of droplet dynamics in complex flows - a review. *Lab on a chip* **4**, 257–264.
- DE BRUIJN, R. A. 1993 Tipstreaming of drops in simple shear flows. *Chem. Eng. Sci.* **48**, 277–284.
- DOMACHUK, P., NGUYEN, H. C., J., E. B., STRAUB, M. & GU, M. 2004 Microfluidic tunable photonic band-gap device. *Appl. Phys. Lett.* **84**, 1838–1840.
- DOSHI, P., COHEN, I., ZHANG, W. W., SIEGEL, M., HOWELL, P., BASARAN, O. A. & NAGEL, S. R. 2003 Persistence of memory in drop breakup: The breakdown of universality. *Science* **302**, 1185–1188.
- EGGERS, J. 1997 Nonlinear dynamics and breakup of free-surface flows. *Rev. Mod. Phys.* **69** (3), 865–929.
- EGGERS, J. 2001 Air entrainment through free-surface cusps. *Phys. Rev. Lett.* **86** (19), 4290–4293.
- EGGLETON, C. D., TSAI, T. M. & STEBE, K. J. 2001 Tip streaming from a drop in the presence of surfactants. *Phys. Rev. Lett.* **87**, 048302.
- FERNANDEZ, J. M. & HOMS, G. M. 2003 Viscous fingering with chemical reaction: effect of in-situ production of surfactants. *J. Fluid Mech.* **480**, 267–281.
- FERNANDEZ, J. M. & HOMS, G. M. 2004 chemical reaction-driven tip-streaming phenomena in a pendant drop. *Phys. Fluids* **16**, 2548–2555.
- FITT, A. D., FURUSAWA, K., MONRO, T. M. & PLEASE, C. P. 2001 Modeling the fabrication of hollow fibers: capillary drawing. *J. Lightwave Tech.* **19** (12), 1924–1931.
- GANAN-CALVO, A. M. & GORDILLO, J. M. 2001 Perfectly monodisperse microbubbling by capillary flow focusing. *Phys. Rev. Lett.* **87**, 274501.
- GANAN-CALVO, A. M., PEREZ-SABORID, M., LOPEZ-HERRERA, J. M. & GORDILLO, J. M. 2004 Steady high viscosity liquid micro-jet production and fiber spinning using co-flowing gas conformation. *Eur. Phys. J. B* **39**, 131–137.

- GARSTECKI, P., FUERSTMANN, M. J. & WHITESIDES, G. M. 2005a Nonlinear dynamics of a flow-focusing bubble-generator: An inverted dripping faucet. *Phys. Rev. Lett.* **94**, 234502.
- GARSTECKI, P., STONE, H. A. & WHITESIDES, G. M. 2005b Mechanism for flow-rate controlled breakup in confined geometries: A route to monodisperse emulsions. *Phys. Rev. Lett.* **94**, 164501.
- GRACE, P. 1982 Dispersion phenomena in high viscosity immiscible fluid systems and application of static mixers as dispersion devices in such systems. *Chem. Eng. Commun.* **14**, 225–239.
- HANSEN, C. L., SKORDALAKES, E., BERGER, J. M. & QUAKE, S. R. 2002 A robust and scalable microfluidic metering method that allows protein crystal growth by free interface diffusion. *Proc. Nat. Acad. Sci.* **99**, 16531–16536.
- HU, Y. T., PINE, D. J. & LEAL, L. G. 2000 Drop deformation, breakup, and coalescence with compatibilizer. *Phys. Fluids* **12**, 484–489.
- JEONG, J.-T. & MOFFATT, H. K. 1992 Free-surface cusps associated with flow at low reynolds number. *J. Fluid Mech.* **241**, 1–22.
- JOANICOT, M. & AJDARI, A. 2005 Applied physics - droplet control for microfluidics. *Science* **309**, 887–888.
- JOSEPH, D. D., NELSON, J., RENARDY, M. & RENARDY, Y. 1991 Two-dimensional cusped interfaces. *J. Fluid. Mech.* **223**, 383–409.
- KRECHETNIKOV, R. & HOMSY, G. M. 2004 On physical mechanisms in chemical reaction-driven tip-streaming. *Phys. Fluids* **16**, 2556–2566.
- LEE, S. H. & LEAL, L. G. 1982 The motion of a sphere in the presence of a deformable interface. ii. a numerical study of the translation of a sphere normal to an interface. *J. Colloid. Interface Science* **87**, 81–106.
- LEPPINEN, D. & LISTER, J. R. 2003 Capillary pinch-off in inviscid fluids. *Phys. Fluids* **15**, 568–578.
- LI, H., HALSEY, T. C. & LOBKOVSKY, A. 1994 Singular shape of an electric drop in an electric or magnetic field. *Europhys. Lett.* **27**, 575–580.
- LIMAT, L. & STONE, H. 2004 Three-dimensional lubrication model of a contact line corner singularity. *Europhys. Lett.* **65**, 365–371.
- LISTER, J. R. 1989 Selective withdrawal from a viscous two-layer system. *J. Fluid Mech.* **198**, 231–254.
- LORENCEAU, E., RESTAGNO, F. & QUERE, D. 2003 Fracture of a viscous liquid. *Phys. Rev. Lett.* **90** (184501).
- LORENCEAU, E., UTADA, A. S., LINK, D. R., CRISTOBAL, G., JOANICOT, M. & WEITZ, D. A. 2005 Generation of polyerosomes from double-emulsions. *Langmuir* **21**, 9183–9186.
- LUCCHETTA, E. M., LEE, J. H., FU, L. A., PATEL, N. H. & ISMAGILOV, R. F. 2005 Dynamics of drosophila embryonic patterning network perturbed in space and time using microfluidics. *Nature* **434**, 1134–1138.
- NAVOT, Y. 1999 Critical behavior of drop breakup in axisymmetric viscous flow. *Phys. Fluids* **11**, 990–996.
- RALLISON, J. M. 1984 The deformation of small viscous drops and bubbles in shear flows. *Ann. Rev. Fluid Mech.* **16**, 45–66.
- RALLISON, J. M. & ACRIVOS, A. 1978 A numerical study of the deformation and burst of a viscous drop in an extensional flow. *J. Fluid Mech.* **89** (1), 191–200.
- REZNIK, S. N., YARIN, A. L., THERON, A. & ZUSSMAN, E. 2004 Transient and steady shapes of droplets attached to a surface in a strong electric field. *J. Fluid Mech.* **516**, 349–377.
- SHELLEY, A., BONTOUX, N. & STONE, H. A. 2003 Formation of dispersions using flow focusing in microchannels. *Appl. Phys. Lett.* pp. 364–366.
- SIEROU, A. & LISTER, J. R. 2003 Self-similar solutions for viscous capillary pinch-off. *J. Fluid Mech.* **497**.
- SONG, H., TICE, J. D. & ISMAGILOV, R. F. 2003 A microfluidic system for controlling reaction networks in time. *Angewandte chemie* **42**, 768–772.
- STONE, H. A. 1994 Dynamics of drop deformation and breakup in viscous fluids. *Ann. Rev. Fluid Mech.* **65**, 65–102.
- STROGATZ, S. H. 1994 *Nonlinear dynamics and chaos*. Perseus Books Publishing, Cambridge, MA.

- TAKEUCHI, S., GARSTECKI, P., WEIBEL, D. B. & WHITESIDES, G. M. 2005 An axisymmetric flow-focusing microfluidic device. *Advanced Materials* **17**, 1067–1068.
- TAYLOR, G. I. 1934 The formation of emulsions in definable fields of flow. *Proc. Roy. Soc. A* **CXLVI**, 501–523.
- TAYLOR, G. I. 1964*a* Conical free surfaces and fluid interfaces. *Proc. 11th Int. Cong. Appl. Mech.* pp. 790–796.
- TAYLOR, G. I. 1964*b* Disintegration of water drops in an electric field. *Proc. Roy. Soc. London A*. **280**, 383–397.
- TICE, J. D., LYON, A. D. & ISMAGILOV, R. F. 2004 Effects of viscosity on droplet formation and mixing in microfluidic channels. *Analytica Chimica Acta* **507**, 73–77.
- UMBANHOWAR, P., PRASAD, V. & WEITZ, D. A. 2000 Monodisperse emulsion generation via drop break-off in a co-flowing stream. *Langmuir* **16**, 347–350.
- UTADA, A. S., LORENCEAU, E., LINK, D. R., KAPLAN, P. D., A., S. H. & A., W. D. 2005 Monodisperse double emulsions generated from a microcapillary device. *Science* **308**, 537–541.
- WOLFE, D. B., CONROY, R. S., GARSTECKI, P., MAYERS, B. T., FISCHBACH, M. A., PAUL, K. E., PRENTISS, M. & WHITESIDES, G. M. 2004 Dynamic control of liquid-core/liquid-cladding optical waveguides. *Proc. Nat. Acad. Sci.* **101**, 12434–12438.
- WYMAN, J., DILLMORE, S., W., M., M., G., MRKSICH, M. & R., N. S. 2004 Microencapsulation of islets of langerhans via selective withdrawal to achieve immunoisolation. APS March Meeting, W9.008.
- ZHANG, W. W. 2004 Viscous entrainment from a nozzle: Singular liquid spouts. *Phys. Rev. Lett.* p. 184502.
- ZHANG, W. W. & LISTER, J. R. 1999 Similarity solutions for capillary pinch-off in fluids of differing viscosity. *Phys. Rev. Lett.* **83**, 1151–1154.
- ZUBAREV, N. M. 2002 Self-similar solutions for conic cusps formation at the surface of dielectric liquids in electric fields. *Phys. Rev. E* **65**, 055301.